Geophysical Journal International

Geophys. J. Int. (2015) **202,** 163–174 doi: 10.1093/gji/ggv115

GJI Mineral physics, rheology, heat flow and volcanology

Time-dependent displacement and stress fields due to shear and tensile faults in a transversely isotropic viscoelastic half-space

Amirhossein Molavi Tabrizi and Ernian Pan

Department of Civil Engineering, University of Akron, Akron, OH 44325*, USA. E-mail: pan2@uakron.edu*

Accepted 2015 March 4. Received 2015 February 9; in original form 2014 December 30

SUMMARY

Viscoelastic behaviour of materials in nature is observed in post-event deformations due to seismic or volcanic activities. In this paper, by adopting the correspondence principle, we propose an inelastic model to predict first the Laplace-domain response of a transversely isotropic viscoelastic half-space due to a shear or tensile fault of polygonal shape. The displacement and stress fields in the time domain are then obtained using an efficient and accurate algorithm for the inverse Laplace transform. Numerical examples are presented to validate the proposed solution and to show the viscoelastic displacement and stress fields due to a strike-slip, dip-slip and tensile fault of rectangular shape. The obtained results indicate that both viscoelasticity and transverse isotropy play significant roles in the viscoelastic response of the half-space due to faults, which could be used as benchmarks for the future numerical analysis of realistic post-seismic or volcanic event.

Key words: Geomechanics; Elasticity and anelasticity; Fault zone rheology; Fractures and faults.

1 INTRODUCTION

Space geodesy enables us to gain a better understanding of delayed post-event deformations of the Earth's surface (Fialko 2004). However, based on the enhanced observations of interferometric synthetic aperture radar (InSAR) and global positioning system (GPS), the existing elastic models fail to predict the real deformation fields on the surface of the Earth. For instance these models cannot reproduce the observed uplifts (Piombo *et al.* 2007). One way to overcome this flaw is to consider a viscoelastic lithosphere in post-seismic or volcanic events. The viscoelastic model can be defined in the way that the source function in time and the relaxation of deformation and stress fields in the inelastic media over time control the post-event transients. The correspondence principle can be adopted to take care of the complicated time convolution in the time domain (Christensen 1982). The correspondence principle enables us to solve the equivalent elastic problem in the Laplace domain by replacing the elastic moduli with the Laplace transformed complex moduli. Therefore, the responses in the time domain can be obtained by utilizing an efficient inverse Laplace transform algorithm should the corresponding elastic problem be solved analytically.

The deformation and stress responses of an elastic or viscoelastic half-space due to dislocation sources have been investigated by many researchers. Nur & Mavko (1974) considered an elastic lithosphere overlying a viscoelastic half-space (the asthenosphere) to study the post-seismic deformation due to sudden dislocation sources. Singh & Rosenman (1974) found the quasi-static deformation of a viscoelastic half-space due to a displacement dislocation. Okada (1985) derived the exact closed-form surface deformations due to shear and tensile faults in an isotropic elastic (IE) half-space. Okada later presented the closed-form solution for the internal deformations and strains (Okada 1992). Piombo *et al.* (2007) extended Okada's elastic solutions to the corresponding viscoelastic isotropic half-space. Hetland & Hager (2005, 2006) utilized the correspondence principle to find the inverse Laplace transforms for general linear viscoelastic rheologies. They presented the deformation field near an infinite strike-slip fault in an elastic layer overlaying a viscoelastic half-space. Recently, Chen *et al.* (2009) derived the semi-analytical solution for a multilayered viscoelastic pavement due to a surface loading.

Although the assumption of isotropy could be suitable for crystalline basement rocks, it fails to describe accurately the behaviour of sedimentary rock masses. These types of rocks are best described by a transversely isotropic material model with the sedimentary plane being parallel to the isotropic plane (Amadei 1996; Wang & Liao 1998; Gercek 2007). Pan *et al.* (2014) extended Okada's solution (Okada 1985, 1992) to the corresponding transversely isotropic half-space with a general polygonal fault and showed that rock anisotropy could significantly affect the displacement and strain fields induced by the fault.

In this paper, the analytical solution of a transversely isotropic viscoelastic (TIV) half-space due to the shear and tensile faults is derived. We emphasize that since the half-space is assumed to be homogeneous, the effect of material layering, that is an elastic lithosphere overlying a viscoelastic half-space, is not considered. In deriving our solution, the correspondence principle is first utilized

to find the displacement and stress solutions in the Laplace domain. Then, by using the inverse Laplace transform algorithm of Honig & Hirdes (1984), the viscoelastic response in the time domain is obtained. This paper is organized as follows: The geometry of the problem and the proposed rheology model are defined in Section 2. A brief introduction to the inverse Laplace transform algorithms and the features of the adopted algorithm in this work are also presented in this section. Numerical examples are carried in Section 3 to validate the proposed viscoelastic solution and to further demonstrate the influence of the transverse isotropy and viscoelasticity on the deformation and stress fields in the TIV half-space. Conclusions are drawn in Section 4. In this paper, the following abbreviations are used for simplicity: AV, anisotropic viscoelastic; IE, isotropic elastic; IV, isotropic viscoelastic; TIE, transversely isotropic elastic; TIV, transversely isotropic viscoelastic.

2 PROBLEM DESCRIPTION

We consider a fault of rectangular shape in a transversely isotropic and viscoelastic (TIV) homogenous half-space. The geometry of the problem is shown in Fig. 1 which is similar to Okada (1992), Piombo *et al.* (2007) and Pan *et al.* (2014). In the adopted coordinate system, the x_1–x_2 plane is the free surface of the half-space and $x_3 \leq 0$ is the problem domain. The axis of symmetry of the TIV material is assumed to be parallel to the x_3-axis. The strike-slip, dip-slip and tensile components of the dislocation are, respectively, U_s, U_d and U_t, representing the movement of the hanging wall relative to the foot wall of the fault. The strike direction and the dip angle of the fault are represented by ϕ and δ, respectively.

2.1 Viscoelastic constitutive relation

The general constitutive relation for a linear anisotropic viscoelastic (AV) medium can be expressed as (Christensen 1982),

$$\sigma_{ij}(\mathbf{x}, t) = \Psi_{ijkl}(\mathbf{x}, t) * \dot{\varepsilon}_{kl}(\mathbf{x}, t), \tag{1}$$

where $\mathbf{x}$ is the position vector, t is the time variable, Ψ_{ijkl} is the fourth-order relaxation function tensor, and the star '$*$' denotes the time convolution. A dot above the variable indicates the time differentiation, and the summation from 1 to 3 is implied over the repeated indices. Similar to the work by Carcione (1990), we now define the relaxation matrix as,

$$\mathbf{\Psi}_{\mathrm{AV}} = \begin{bmatrix} \psi_{11} & \psi_{12} & \psi_{13} & c_{14} & c_{15} & c_{16} \\ & \psi_{22} & \psi_{23} & c_{24} & c_{25} & c_{26} \\ & & \psi_{33} & c_{34} & c_{35} & c_{36} \\ & & & c_{44}\chi_2 & c_{45}\chi_2 & c_{46}\chi_2 \\ & Sym. & & & c_{55}\chi_2 & c_{56}\chi_2 \\ & & & & & c_{66}\chi_2 \end{bmatrix} H(t), \tag{2}$$

where $\mathbf{\Psi}_{\mathrm{AV}}$ is the relaxation matrix for an AV material and $H(t)$ is the Heaviside function. The elements of the relaxation matrix are,

$$\begin{cases} \psi_{ij} = c_{ij} - D + \left(D - \frac{4}{3}G\right)\chi_1 + \frac{4}{3}G\chi_2 & \text{if} \quad i = j \\ \psi_{ij} = c_{ij} - D + 2G + \left(D - \frac{4}{3}G\right)\chi_1 - \frac{2}{3}G\chi_2 & \text{if} \quad i \neq j \end{cases} \tag{3}$$

with

$$D = (c_{11} + c_{22} + c_{33})/3 \tag{4}$$

$$G = (c_{44} + c_{55} + c_{66})/3. \tag{5}$$

Furthermore, in eqs (2) and (3), matrix c_{ij} represents the space-dependent stiffness and

$$\chi_v = 1 - \sum_{l=1}^{L_v} \left(1 - \frac{\tau_{\varepsilon l}^v}{\tau_{\sigma l}^v}\right)\left(1 - e^{-t/\tau_{\sigma l}^v}\right) \quad v = 1, 2 \tag{6}$$

are the relaxation functions with $\tau_{\varepsilon l}^v$ and $\tau_{\sigma l}^v$ being the material relaxation times for the lth mechanism and L_v being the total number of relaxation mechanisms. It is noted that the relaxation matrix $\mathbf{\Psi}_{\mathrm{AV}}$ is formed in such a way that the trace and deviatoric components

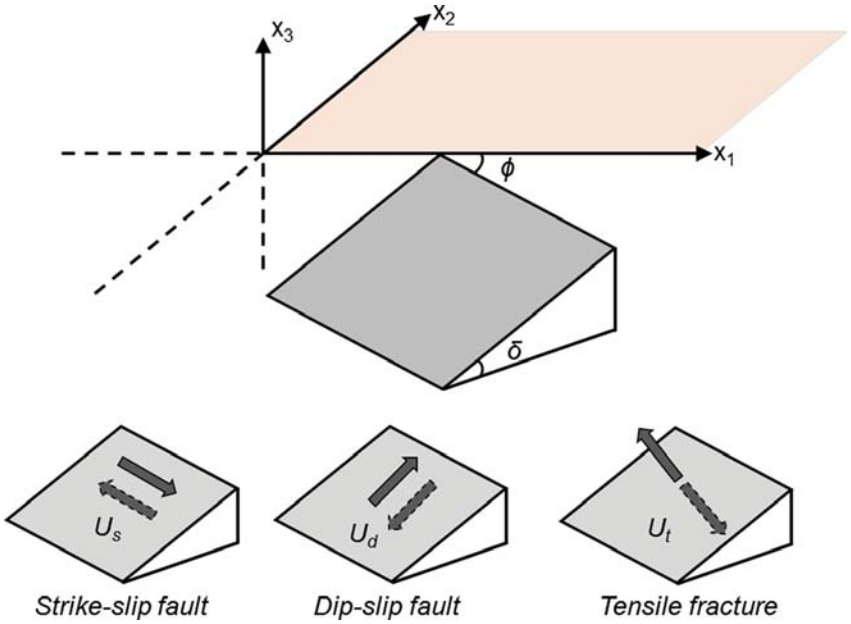

Figure 1. Geometry of a rectangular fault with three types of discontinuities U_s, U_d and U_t in a transversely isotropic viscoelastic half-space (with x_1–x_2 being the plane of isotropy and $x_3 = 0$ being the free surface). The strike direction and the dip angle of the fault are represented by ϕ and δ, respectively.

of the stress tensor depend on the time variable through the kernels χ_1 and χ_2, respectively. The trace of the stress tensor is an invariant upon the transformation of the coordinate system implying that the hydrostatic stress (one third of the trace) is only related to the function χ_1. Hence, function χ_1 describes the dilatational deformation whereas χ_2 represents the shear deformation (Carcione *et al.* 1988 and Carcione 1990). We should point out that our relaxation functions presented in eq. (6) are similar to but different from those in Carcione (1990). The difference is that in Carcione (1990), time $t = \infty$ (0) corresponds to the elastic (relaxation) limit whilst in eq. (6), $t = 0$ (∞) corresponds to the elastic (relaxation) limit. Thus the adopted relaxation functions in our paper can be reduced to the viscoelastic model frequently used in geophysics for post-seismic deformation analyses, as we will show below when validating our solutions against those by Singh & Rosenman (1974).

For the TIV material, eq. (2) can be reduced to

$$\mathbf{\Psi}_{\rm TIV} = \begin{bmatrix} \psi_{11} & \psi_{12} & \psi_{13} & 0 & 0 & 0 \\ & \psi_{11} & \psi_{13} & 0 & 0 & 0 \\ & & \psi_{33} & 0 & 0 & 0 \\ & & & c_{44}\chi_2 & 0 & 0 \\ & Sym. & & & c_{44}\chi_2 & 0 \\ & & & & & c_{66}\chi_2 \end{bmatrix} H(t), \tag{7}$$

where $\mathbf{\Psi}_{\rm TIV}$ is the relaxation matrix for a TIV material with

$$\begin{cases} \psi_{ij} = c_{ij} - D + \left(D - \frac{4}{3}G\right)\chi_1 + \frac{4}{3}G\chi_2 & \text{if} \quad i = j \\ \psi_{ij} = c_{ij} - D + 2G + \left(D - \frac{4}{3}G\right)\chi_1 - \frac{2}{3}G\chi_2 & \text{if} \quad i \neq j \end{cases} \tag{8}$$

and

$$D = (2c_{11} + c_{33})/3; \quad G = (2c_{44} + c_{66})/3 \tag{9}$$

$$c_{66} = (c_{11} - c_{12})/2. \tag{10}$$

For an isotropic viscoelastic (IV) material, the relaxation matrix $\mathbf{\Psi}_{\rm TIV}$ can be reduced to

$$\mathbf{\Psi}_{\rm IV} = \begin{bmatrix} \psi_{11} & \psi_{12} & \psi_{12} & 0 & 0 & 0 \\ & \psi_{11} & \psi_{12} & 0 & 0 & 0 \\ & & \psi_{11} & 0 & 0 & 0 \\ & & & \psi_{44} & 0 & 0 \\ & Sym. & & & \psi_{44} & 0 \\ & & & & & \psi_{44} \end{bmatrix} \tag{11}$$

$$\begin{aligned} \psi_{11} &= \left(\lambda + \frac{2}{3}\mu\right)\chi_1 + \frac{4}{3}\mu\chi_2 \\ \psi_{12} &= \left(\lambda + \frac{2}{3}\mu\right)\chi_1 - \frac{2}{3}\mu\chi_2 \\ \psi_{44} &= \mu\chi_2, \end{aligned} \tag{12}$$

where $\mathbf{\Psi}_{\rm IV}$ is the relaxation matrix for an IV material and λ and μ are the elastic Lamé constants of the isotropic material.

We remark that at $t = 0$ the relaxation matrices for the AV, TIV and IV will represent the corresponding elastic limit of the problem. This elastic limit corresponds further to the situation where the two relaxation functions in eq. (6) are reduced to unit 1, namely, $\chi_\nu = 1$ ($\nu = 1, 2$). We further point out that, at $t = 0$, the IV material will be reduced to the IE material and the TIV material to the transversely isotropic elastic (TIE) material. Therefore, the solutions presented by Okada (1985, 1992) in the IE half-space and by Pan *et al.* (2014) in the TIE half-space can be utilized to verify the proposed viscoelastic solutions.

Based on the viscoelastic correspondence principle (Christensen 1982), the formulation of the present viscoelastic problem will be equal to the corresponding elastic problem in Laplace domain with Laplace transformed complex material properties. The Laplace transform of a real function f with $f(t) = 0$ for $t < 0$ is

$$F(s) = L\,[f(t)] = \int_0^\infty \mathrm{e}^{-st} f(t)\,\mathrm{d}t. \tag{13}$$

Thus, the constitutive relation eq. (1) in the Laplace domain can be written as

$$\bar{\sigma}_{ij}(\mathbf{x}, s) = s\,\bar{\Psi}_{ijkl}(\mathbf{x}, s)\bar{\varepsilon}_{kl}(\mathbf{x}, s), \tag{14}$$

where s is the Laplace variable and the overbar denotes the function in the Laplace domain. The relaxation functions and relaxation tensor for the TIV materials in the Laplace domain are given as,

$$\bar{\chi}_\nu = \frac{1}{s} - \sum_{l=1}^{L_\nu}\left(1 - \frac{\tau_{\varepsilon l}^\nu}{\tau_{\sigma l}^\nu}\right)\left(\frac{1}{s} - \frac{1}{s + 1/\tau_{\sigma l}^\nu}\right) \qquad \nu = 1, 2 \tag{15}$$

$$\bar{\mathbf{\Psi}}_{\rm TIV} = \begin{bmatrix} \bar{\psi}_{11} & \bar{\psi}_{12} & \bar{\psi}_{13} & 0 & 0 & 0 \\ & \bar{\psi}_{11} & \bar{\psi}_{13} & 0 & 0 & 0 \\ & & \bar{\psi}_{33} & 0 & 0 & 0 \\ & & & c_{44}\bar{\chi}_2 & 0 & 0 \\ & Sym. & & & c_{44}\bar{\chi}_2 & 0 \\ & & & & & c_{66}\bar{\chi}_2 \end{bmatrix} \tag{16}$$

with

$$\begin{cases} \bar{\psi}_{ij} = \frac{c_{ij}}{s} - \frac{D}{s} + \left(D - \frac{4}{3}G\right)\bar{\chi}_1 + \frac{4}{3}G\bar{\chi}_2 & \text{if} \quad i = j \\ \bar{\psi}_{ij} = \frac{c_{ij}}{s} - \frac{D}{s} + \frac{2G}{s} + \left(D - \frac{4}{3}G\right)\bar{\chi}_1 - \frac{2}{3}G\bar{\chi}_2 & \text{if} \quad i \neq j, \end{cases} \tag{17}$$

where D and G are defined by Eq. (9) and Eq. (10) holds for c_{66}. The elastic deformation due to a shear and tensile polygonal fault in a TIE half-space was recently solved by Pan *et al.* (2014). Therefore, making use of these solutions, the displacement and its derivative induced by a strike-slip, dip-slip and tensile fault in a TIV half-space can be expressed in the Laplace transformed domain as

Strike-slip fault,

$$\begin{aligned} \bar{u}_i(\mathbf{x}, s) &= -\bar{U}_s\left\{\cos\phi\bar{U}_{i1}(\mathbf{x}, s) + \sin\phi\bar{U}_{i2}(\mathbf{x}, s)\right\} \\ \bar{u}_{i,j}(\mathbf{x}, s) &= -\bar{U}_s\left\{\cos\phi\bar{U}_{i1,j}(\mathbf{x}, s) + \sin\phi\bar{U}_{i2,j}(\mathbf{x}, s)\right\} \end{aligned} \tag{18}$$

Dip-slip fault,

$$\begin{aligned} \bar{u}_i(\mathbf{x}, s) &= \bar{U}_d\{\sin\phi\cos\delta\bar{U}_{i1}(\mathbf{x}, s) - \cos\phi\cos\delta\bar{U}_{i2}(\mathbf{x}, s) \\ &\quad - \sin\delta\bar{U}_{i3}(\mathbf{x}, s)\} \\ \bar{u}_{i,j}(\mathbf{x}, s) &= \bar{U}_d\{\sin\phi\cos\delta\bar{U}_{i1,j}(\mathbf{x}, s) - \cos\phi\cos\delta\bar{U}_{i2,j}(\mathbf{x}, s) \\ &\quad - \sin\delta\bar{U}_{i3,j}(\mathbf{x}, s)\}. \end{aligned} \tag{19}$$

Tensile fault,

$$\begin{aligned} \bar{u}_i(\mathbf{x}, s) &= \bar{U}_t\{-\sin\phi\sin\delta\bar{U}_{i1}(\mathbf{x}, s) + \cos\phi\sin\delta\bar{U}_{i2}(\mathbf{x}, s) \\ &\quad - \cos\delta\bar{U}_{i3}(\mathbf{x}, s)\} \end{aligned}$$

$$\bar{u}_{i,j}(\mathbf{x},s) = \bar{U}_t\left\{-\sin\phi\sin\delta\bar{U}_{i1,j}(\mathbf{x},s)+\cos\phi\sin\delta\bar{U}_{i2,j}(\mathbf{x},s) - \cos\delta\bar{U}_{i3,j}(\mathbf{x},s)\right\}, \tag{20}$$

where

$$\bar{U}_{ij}(\mathbf{x},s) = \bar{U}^{\infty}_{ij}(\mathbf{x},s)+\bar{U}^{c}_{ij}(\mathbf{x},s), \tag{21}$$

where $\bar{U}_{ij}(\mathbf{x},s)$ is the i-component of the Laplace-domain displacement in the half-space at $\mathbf{x}$ for a given uniform displacement discontinuity in the j-direction on the fault, $\bar{U}^{\infty}_{ij}(\mathbf{x},s)$ is the i-component of the full-space displacement at $\mathbf{x}$ due to the same uniform displacement discontinuity in the j-direction, and $\bar{U}^{c}_{ij}(\mathbf{x},s)$ is the complementary part of the solution satisfying the free surface boundary conditions (Pan *et al.* 2014). Using eqs (18)–(20) with eq. (14), the stress components in the Laplace domain can be obtained.

2.2 Inverse Laplace transform

Based on the formulations presented in the previous section, the displacements and stresses induced by faulting in a TIV half-space can be found in the Laplace domain by the correspondence principle. The next step is to transform these components back to the time domain. Once the solutions are found in the Laplace transformed domain, the time-domain solutions are obtained by carrying out the inverse Laplace transform. In other word, once $F(s)$ is given as in eq. (13), its time-domain expression with $f(t) = 0$ for $t < 0$ can be found by taking the inverse Laplace transform

$$f(t) = L^{-1}[F(s)] = \frac{1}{2\pi i}\int_{\kappa-i\infty}^{\kappa+i\infty} e^{st}F(s)\,ds \tag{22}$$

with $s = \kappa + i\omega$ and κ, ω being real values.

Since in general, the inverse of $F(s)$ cannot be found analytically, numerical methods are needed to carry out the inverse integral in eq. (22). Several numerical algorithms have been proposed to carry out the inverse Laplace transform (Weeks 1966; Dubner & Abate 1968; Stehfest 1970; Durbin 1974; Talbot 1979; De Hoog *et al.* 1982; Honig & Hirdes 1984), and comparisons among different algorithms can be found in Bellman *et al.* (1966), Davies & Martin (1979), Duffy (1993), Cohen (2007) and Kuhlman (2013). In this paper, we use the algorithm presented by Honig & Hirdes (1984) for the numerical inverse Laplace transform. The algorithm is based on the Fourier series expansion developed by Dubner & Abate (1968) and Durbin (1974), and is presented briefly below.

By following Durbin (1974), if the Laplace transform of $f(t)$ is $F(s)$ as defined by eq. (13), then its inverse Laplace transform, as defined by eq. (22), can be approximated by the Fourier series expansion in the time interval $[0, 2T]$ as

$$f_N(t) = \frac{e^{\kappa t}}{T}\left[-\frac{1}{2}\mathrm{Re}\{F(\kappa)\}+\sum_{j=0}^{N}\left(\mathrm{Re}\left\{F\left(\kappa+i\frac{j\pi}{T}\right)\right\}\times\cos\left(\frac{j\pi}{T}t\right)-\mathrm{Im}\left\{F\left(\kappa+i\frac{j\pi}{T}\right)\right\}\sin\left(\frac{j\pi}{T}t\right)\right)\right], \tag{23}$$

where κ, T and N are three real parameters which need to be chosen properly. Thus, the accuracy of the original algorithm by Durbin (1974) depends on the discretization and truncation errors related to these parameters. Honig & Hirdes (1984) proposed two different methods for finding the optimal values of these parameters: (1) for fixed N and T, they found the optimum value for κ by equalizing the truncation and discretization error and (2) the optimum value for κ was calculated by minimizing the sum of the absolute values of discretization and truncation errors. Furthermore, Honig & Hirdes (1984) adopted three different algorithms to accelerate the convergence of the Fourier series: ϵ-algorithm, minimum-maximum method and curve-fitting based method. Due to these unique features, we utilize the algorithm of Honig & Hirdes (1984) to carry out the involved inverse Laplace transform numerically to find the displacement and stress components in the time domain. Our numerical examples listed in the Appendix show that this inverse Laplace algorithm is very efficient and accurate.

3 RESULTS AND DISSCUSION

In the first numerical example, the displacement response on the surface of an IV half-space due to a strike-slip vertical fault is studied. The dimension of the fault in the IV medium is 10 km × 10 km with a uniform dislocation $U_s = 50\,H(t)$ cm over the entire fault (Fig. 2). The lower edge of the fault is 12 km below the surface and the strike direction of the fault is parallel to the x_1-axis. We assume that the medium is elastic dilatational and Maxwell deviatoric which satisfying the Poisson condition ($\lambda = \mu$). To apply our viscoelastic model to this simple Maxwell model, we only need to simply set $\chi_1 = 1$ and $\tau^2_\varepsilon = 0$ in the relaxation functions eq. (6). Under these conditions, the other relaxation function χ_2 will be

$$\chi_2 = e^{-t/\tau^2_\sigma}, \tag{24}$$

where τ^2_σ is the relaxation time in shear for the Maxwell model. The viscoelastic displacement components are obtained at a fixed surface point on the IV half-space located at (x_1, x_2, x_3) = (2, 3, 0) km (Fig. 2). The displacement components as functions of

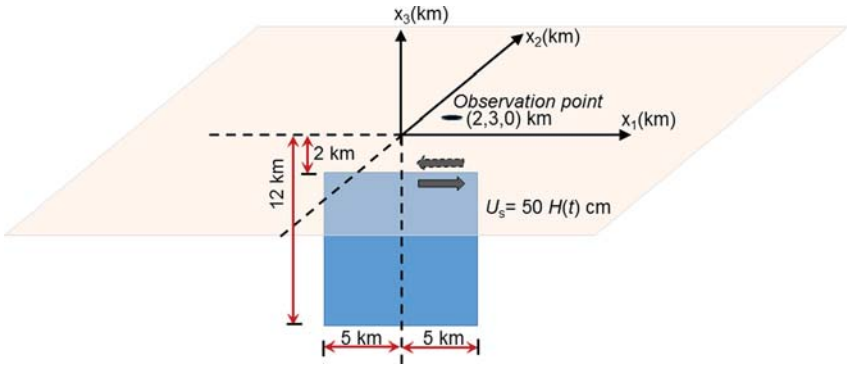

Figure 2. A strike-slip vertical fault of square shape with dimension 10 km × 10 km in an IV half-space. The fault is under a uniform dislocation $U_s = 50$ $H(t)$ cm. The lower edge of the fault is 12 km below the surface and the strike direction of the fault is parallel to the x_1-axis.

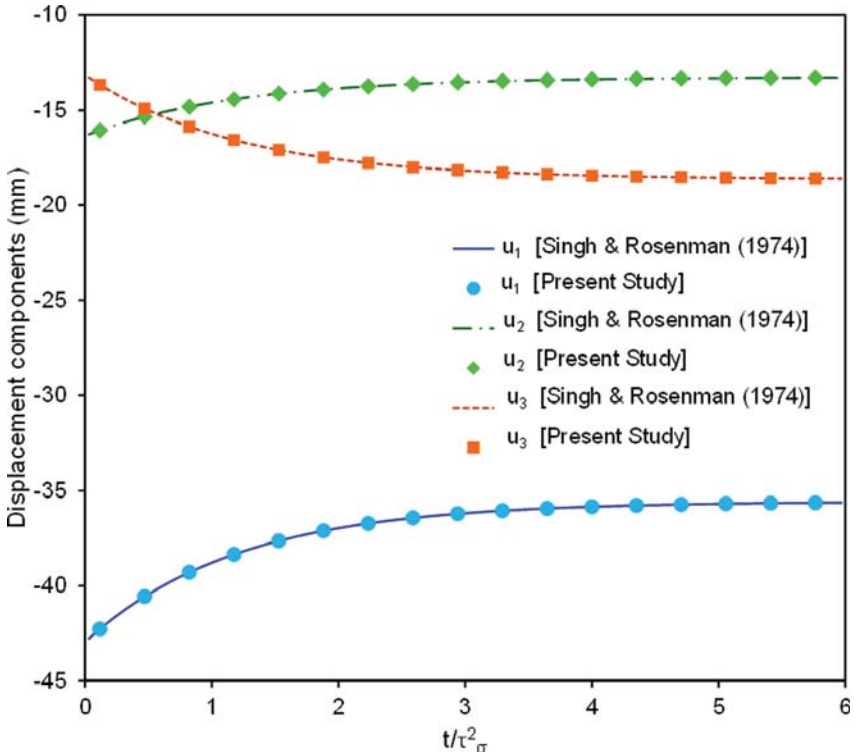

Figure 3. Viscoelastic displacement components u_1, u_2, u_3 versus dimensionless time t/τ_σ^2 at fixed point $(x_1, x_2, x_3) = (2, 3, 0)$ km on the surface of an elastic dilatational and Maxwell deviatoric half-space due to the strike-slip vertical fault in Fig. 2. The analytical solutions by Singh & Rosenman (1974) are also shown for comparison.

dimensionless time are depicted in Fig. 3. As a validation of our calculated displacements via numerical inverse Laplace transform, the analytical solution by Singh & Rosenman (1974) is also presented. It can be deduced that our numerical results are in good agreement with the analytical ones. It can be further observed that with increasing time, the magnitude of the displacement component u_3 monotonically increases while both u_1 and u_2 monotonically decrease (in magnitude), and that all the three displacement components converge to their corresponding limit values when the dimensionless time is about five times of the relaxation time.

In the second numerical example, we present the viscoelastic displacement fields due to a rectangular fault in a TIV half-space made of clayshale. The rectangular fault has a dimension of 12 km × 8 km and it is under a uniform dislocation $U_s = 50\ H(t)$ cm (or $U_d = 50\ H(t)$ cm or $U_t = 50\ H(t)$ cm) (Fig. 4). The lower edge of the fault is 10 km below the surface and the strike direction of the fault is parallel to x_1-axis. The dip angle is $\delta = 40^\circ$ and the field point is fixed at $(x_1, x_2, x_3) = (25, 15, -5)$ km. The stiffness coefficients and relaxation parameters for the TIV (with IV being its special case) medium are taken from Carcione (1990) and are listed in Table 1.

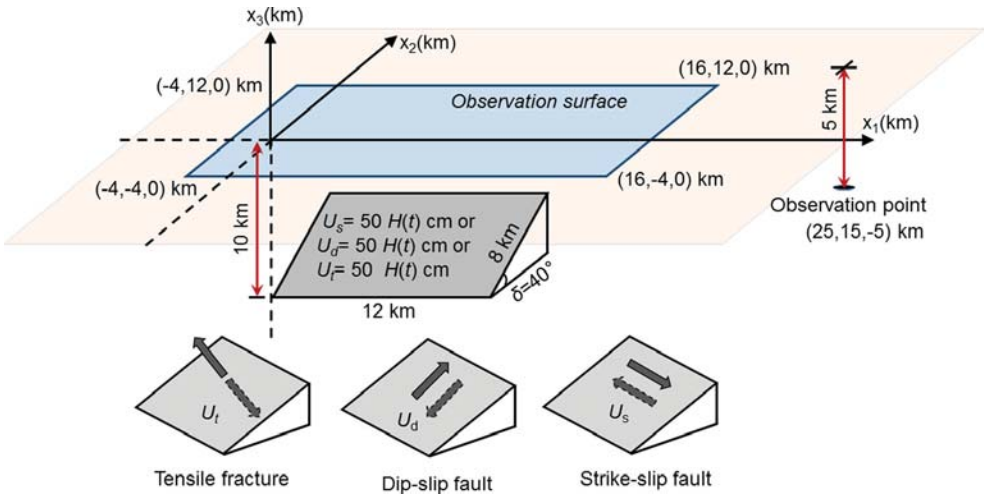

Figure 4. A rectangular fault of dimension 12 km × 8 km under a uniform dislocation $U_s = 50\ H(t)$ cm (or $U_d = 50\ H(t)$ cm or $U_t = 50\ H(t)$ cm) in an IV or TIV half-space. The lower edge of the fault is 10 km below the surface and the strike direction of the fault is parallel to the x_1-axis. The dip angle is $\delta = 40^\circ$. The field point is fixed at $(x_1, x_2, x_3) = (25, 15, -5)$ km for Figs 5 and 6 and the observation domain is a rectangle on the surface of the half-space with -4 km $< x_1 < 16$ km and -4 km $< x_2 < 12$ km for Figs 7–9.

Table 1. Elastic stiffness coefficients and relaxation parameters for TIV, IV and IV (Voigt) clayshale.

Elastic stiffness (GPa)	c_{11}	c_{12}	c_{13}	c_{33}	c_{44}	c_{66}
Clayshale (TIV)	66.6	19.7	39.4	39.9	10.9	23.4
Clayshale (IV)	39.9	18.1	18.1	39.9	10.9	10.9
Clayshale (IV) Voigt average	59.8	31.8	31.8	59.8	14.0	14.0
Relaxation parameters (s)	$\tau^1_{\varepsilon l}$		$\tau^1_{\sigma l}$	$\tau^2_{\varepsilon l}$		$\tau^2_{\sigma l}$
1	0.0332577		0.0304655	0.0352443		0.0287482
2	0.0033257		0.0030465	0.0029370		0.0023957

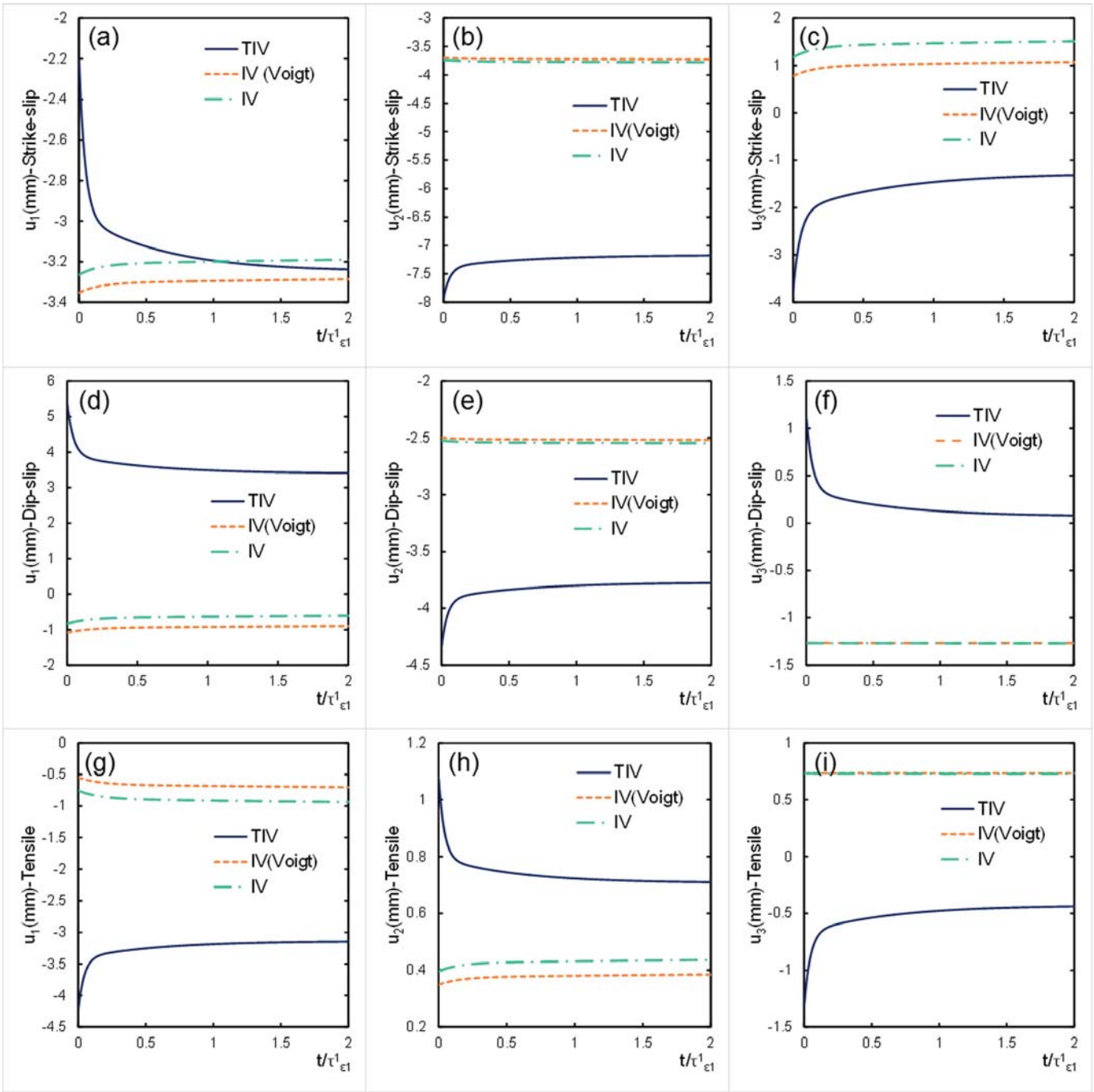

Figure 5. Viscoelastic displacement components as a function of $t/\tau^1_{\varepsilon 1}$ at fixed internal point $(x_1, x_2, x_3) = (25, 15, -5)$ km for the three different types of faults. The first row (a–c) is the displacement induced by a strike-slip fault, the second row (d–f) is the one by a dip-slip fault and the third row (g–i) is the one by a tensile fault. The three curves in each figure correspond to those in the TIV material with solid lines, in the IV material using Voigt average model with dotted lines, and in the IV material with dashed-dotted lines. All the material properties are listed in Table 1.

Table 2. Comparison of the present solutions at the fixed internal point $(x_1, x_2, x_3) = (25, 15, -5)$ km for IV and TIV half-spaces at time $t \approx 0$ with the elastic solutions by Okada's (1992) in IE and Pan *et al.* (2014) in TIE half-spaces.

	Fault type	Strike-slip			Dip-slip			Tensile		
	Displacement (mm)	u_1	u_2	u_3	u_1	u_2	u_3	u_1	u_2	u_3
IV material	Okada (1992)	−3.2642	−3.7373	1.1749	−0.8319	−2.5241	−1.2683	−0.7542	0.3966	0.7325
	IV at $t \approx 0$	−3.2638	−3.7374	1.1766	−0.8308	−2.5242	−1.2683	−0.7551	0.3968	0.7325
	IV(Voigt) at $t \approx 0$	−3.3530	−3.6987	0.7803	−1.0835	−2.5003	−1.2642	−0.5461	0.3490	0.7342
TIV material	Pan *et al.* (2014)	−2.1865	−7.9182	−3.7736	5.3771	−4.3373	1.1136	−4.2437	1.0799	−1.3198
	TIV at $t \approx 0$	−2.2045	−7.9065	−3.7386	5.3438	−4.3275	1.0963	−4.2242	1.0729	−1.3051

Table 3. Viscoelastic displacement components (in mm) at $(x_1, x_2, x_3) = (25, 15, -5)$ km due to the three different types of faults in the TIV half-space at different times.

$t/\tau^1_{\varepsilon 1}$	Strike-slip			Dip-slip			Tensile		
	u_1 (mm)	u_2 (mm)	u_3 (mm)	u_1 (mm)	u_2 (mm)	u_3 (mm)	u_1 (mm)	u_2 (mm)	u_3 (mm)
0.001	−2.2046	−7.9065	−3.7387	5.3438	−4.3275	1.0963	−4.2242	1.0729	−1.3051
0.010	−2.3510	−7.8115	−3.4530	5.0748	−4.2481	0.9563	−4.0675	1.0168	−1.1857
0.100	−2.9341	−7.4124	−2.2010	3.9846	−3.9372	0.3881	−3.4471	0.8050	−0.7011
0.200	−3.0397	−7.3310	−1.9125	3.7815	−3.8821	0.2820	−3.3387	0.7714	−0.6105
0.500	−3.1249	−7.2653	−1.6669	3.6202	−3.8368	0.1966	−3.2539	0.7444	−0.5376
1.000	−3.1944	−7.2116	−1.4600	3.4896	−3.8001	0.1258	−3.1863	0.7229	−0.4773
2.000	−3.2380	−7.1769	−1.3136	3.4090	−3.7766	0.0806	−3.1464	0.7100	−0.4389
4.000	−3.2474	−7.1690	−1.2725	3.3927	−3.771	0.0705	−3.1393	0.7073	−0.4303
4.800	−3.2477	−7.1688	−1.2710	3.3925	−3.7710	0.0703	−3.1392	0.7073	−0.4301
5.000	−3.2477	−7.1688	−1.2708	3.3925	−3.7710	0.0703	−3.1392	0.7073	−0.4301

To investigate the effect of transverse isotropy, the displacement fields for IV clayshale are also presented. Two different IV media are used with their stiffness constants being obtained using two different approaches. In the first approach, the material properties for IV clayshale are directly taken from Carcione (1990) as listed in the row named 'Clayshale (IV)' in Table 1. In the second approach, the equivalent IV stiffness constants are calculated using the Voigt average method (Pan *et al.* 2014). In other words, the Voigt average moduli are calculated using the following formulations once the TIE material properties are given.

$$\lambda_{\text{voigt}} = \frac{c_{11} + c_{33} + 5c_{12} + 8c_{13} - 4c_{44}}{15}$$
$$\mu_{\text{voigt}} = \frac{7c_{11} + 2c_{33} - 5c_{12} - 4c_{13} + 12c_{44}}{30}. \tag{25}$$

This IV material properties are listed in Table 1 in the row named 'Clayshale (IV) Voigt average'.

At the fixed observation point $(x_1, x_2, x_3) = (25, 15, -5)$ km, the time-dependent displacement components vs. normalized time for different types of faults are presented in Fig. 5. It is observed from Fig. 5 that while the two IV material models predict very similar displacements with roughly the same values for the given fault type, the TIV material model predicts completely different displacements as compared to the IV models. This demonstrates that if the rock material under consideration is TIV, use of an IV model would predict completely wrong time-dependent displacements induced by faults. We further notice that all displacement components are either monotonically decrease or monotonically increase, and are finally convergent to their limiting values.

We further mention that we have validated our solutions at the fixed internal point $(x_1, x_2, x_3) = (25, 15, -5)$ km in the corresponding elastic half-space, which are achieved from our viscoelastic models by taking the limit at $t/\tau^1_{\varepsilon 1} \approx 0$. For the isotropic case, our IV and IV (Voigt) models at $t/\tau^1_{\varepsilon 1} \approx 0$ yield the elastic displacements very close to those in Okada (1992), and for the transversely isotropic case, the displacements from our TIV model are nearly equal to those in Pan *et al.* (2014). The comparison of these elastic displacement components are presented in Table 2, with the elastic material properties being those listed in Table 1. Furthermore, listed in Table 3 are the viscoelastic displacement components induced by the three different types of faults in the TIV half-space at different times for future reference (accurate to the listed five digits). It can be observed from this table that the viscoelastic displacement components all approach their convergent values at $t/\tau^1_{\varepsilon 1} \approx 4.5$.

The hydrostatic, effective, and maximum shear stresses at fixed point $(x_1, x_2, x_3) = (25, 15, -5)$ km due to different types of faults are shown in Fig. 6 as functions of time. The hydrostatic stress (σ_{h}), effective stress (σ_{e}) and maximum shear (τ_{m}) stresses are defined, respectively, as

$$\sigma_{\text{h}} = (\sigma_{11} + \sigma_{22} + \sigma_{33})/3$$
$$\sigma_{\text{e}} = \left[0.5\left\{(\sigma_{11} - \sigma_{22})^2 + (\sigma_{22} - \sigma_{33})^2 + (\sigma_{33} - \sigma_{11})^2\right\} + 3\left(\sigma_{12}^2 + \sigma_{23}^2 + \sigma_{13}^2\right)\right]^{0.5}$$
$$\tau_{\text{m}} = \max\left\{\left|\frac{\sigma_1 - \sigma_3}{2}\right|, \left|\frac{\sigma_2 - \sigma_3}{2}\right|, \left|\frac{\sigma_1 - \sigma_2}{2}\right|\right\}, \tag{26}$$

where σ_1, σ_2, and σ_3 are principal stress components. Comparing the variation of the stresses in Fig. 6 to that of the displacements in Fig. 5, we notice that: (1) the stresses from the three viscoelastic models are all different; even the two IV models predict different stress variations; (2) while the hydrostatic stress either monotonically increases or monotonically decreases with normalized time

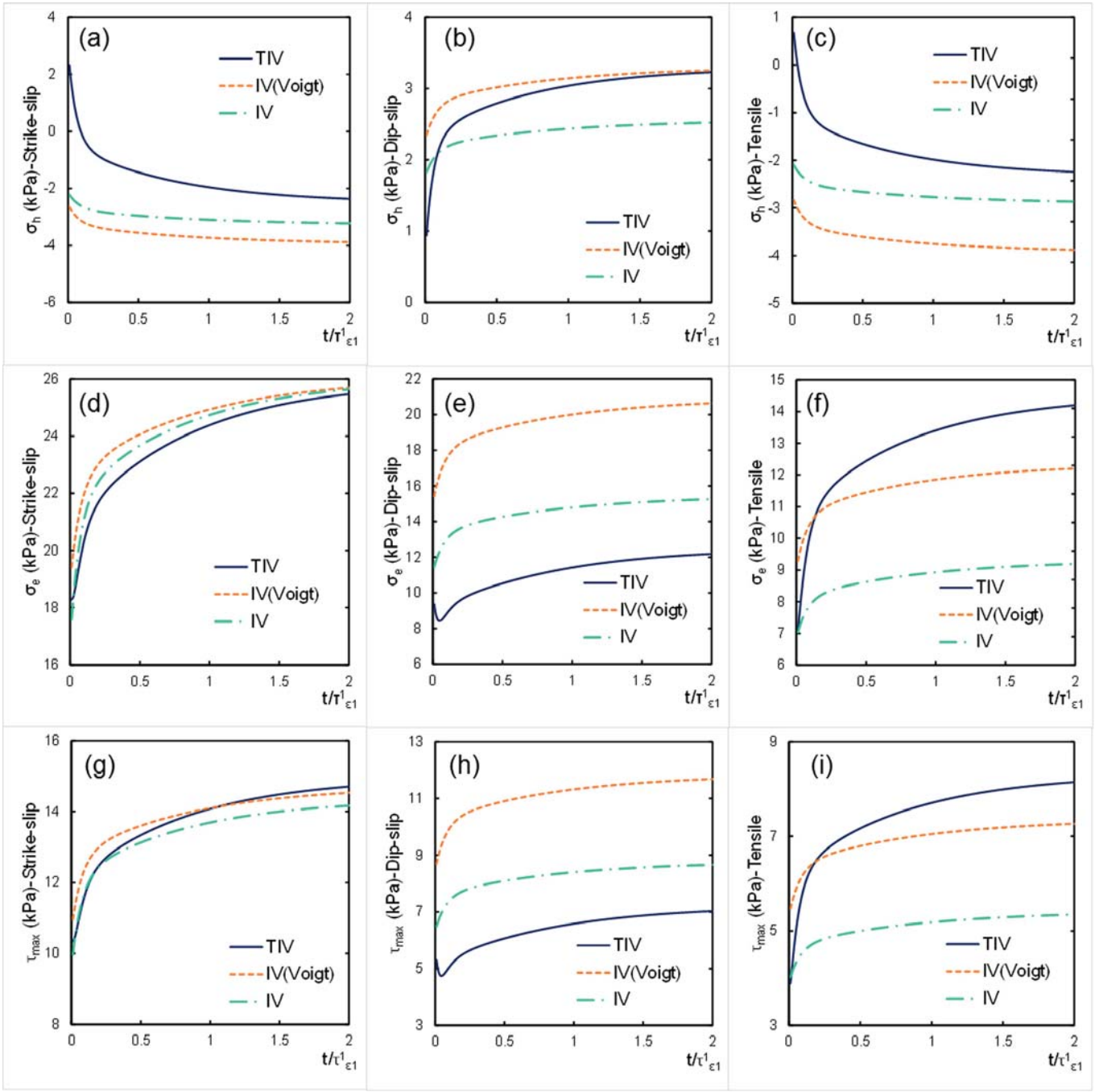

Figure 6. Hydrostatic stress (σ_h), effective stress (σ_e), and maximum shear stress ($\tau_{max} \equiv \tau_m$) as functions of $t/\tau^1_{\varepsilon 1}$ at fixed internal point $(x_1, x_2, x_3) = (25, 15, -5)$ km induced by different types of faults in three different viscoelastic half-spaces. The first row (a–c) is the hydrostatic stress due to the strike-slip, dip-slip and tensile faults. The second row (d–f) is the effective stress due to the strike-slip, dip-slip and tensile faults. The third row (g–i) is the maximum shear stress due to strike-slip, dip-slip and tensile faults. The three curves in each figure correspond to those in the TIV half-space with solid lines, in the IV half-space using Voigt average model with dotted lines, and in the IV half-space with dashed-dotted lines. All the half-space material properties are listed in Table 1.

(Figs 6a–c), the variation of the effective stress and maximum shear stress is peculiar (Figs 6d–h; Table 4) in the TIV half-space. More specifically, under either a strike-slip or a dip-slip faulting, the minimum of the induced effective stress and maximum shear stress is not at the elastic limit $t = 0$, but at a later time when the material experiences viscoelastic deformation (Table 4). We further remark that since the maximum shear stress is the key stress component in Mohr–Coulomb failure criterion and that other stresses are also increasing with increasing time, failure induced by a faulting may not occur immediately at time $t = 0$ in the viscoelastic materials; rather it may be delayed due to the viscoelastic effect. Similar phenomena were observed for crack propagation in viscoelastic materials (Knauss 1970; Wnuk & Knauss 1970). Finally in Table 4 (accurate to the listed five digits), we have listed the time-dependent hydrostatic stress, effective stress, and maximum shear stress at fixed point $(x_1, x_2, x_3) = (25, 15, -5)$ km induced by different types of faults in the TIV half-space for future reference. It is clearly observed from Table 4 that all these stresses converge when the dimensionless time

Table 4. Time-dependent hydrostatic stress (σ_h), effective stress (σ_e), and maximum shear stress (τ_m) in (kPa) at fixed internal point $(x_1, x_2, x_3) = (25, 15, -5)$ km induced by different types of faults in the TIV half-spaces.

$t/\tau^1_{\varepsilon 1}$	Strike-slip			Dip-slip			Tensile		
	σ_h (kPa)	σ_e (kPa)	τ_m (kPa)	σ_h (kPa)	σ_e (kPa)	τ_m (kPa)	σ_h (kPa)	σ_e (kPa)	τ_m (kPa)
0.001	2.8440	18.4245	10.3917	0.6701	10.0759	5.7491	0.9918	6.6758	3.7226
0.010	2.3246	18.2885	10.3420	0.9407	9.3620	5.3071	0.6785	7.0559	3.8921
0.100	−0.1239	20.3375	11.6958	2.1728	8.8406	5.0440	−0.8252	10.1633	5.8622
0.200	−0.8064	21.6652	12.4890	2.4956	9.6015	5.5130	−1.2567	11.3011	6.5237
0.500	−1.4347	23.1100	13.3375	2.7928	10.5363	6.0680	−1.6546	12.4398	7.1675
1.000	−1.9583	24.3870	14.0796	3.0396	11.4227	6.5862	−1.9850	13.4081	7.7056
2.000	−2.3658	25.4722	14.7059	3.2306	12.1838	7.0290	−2.2429	14.2011	8.1432
4.000	−2.5068	25.8879	14.9452	3.2973	12.4661	7.1930	−2.3326	14.4984	8.3076
4.800	−2.5145	25.9134	14.9599	3.3012	12.4824	7.2025	−2.3375	14.5164	8.3176
5.000	−2.5155	25.9167	14.9618	3.3017	12.4845	7.2037	−2.3382	14.5188	8.3190

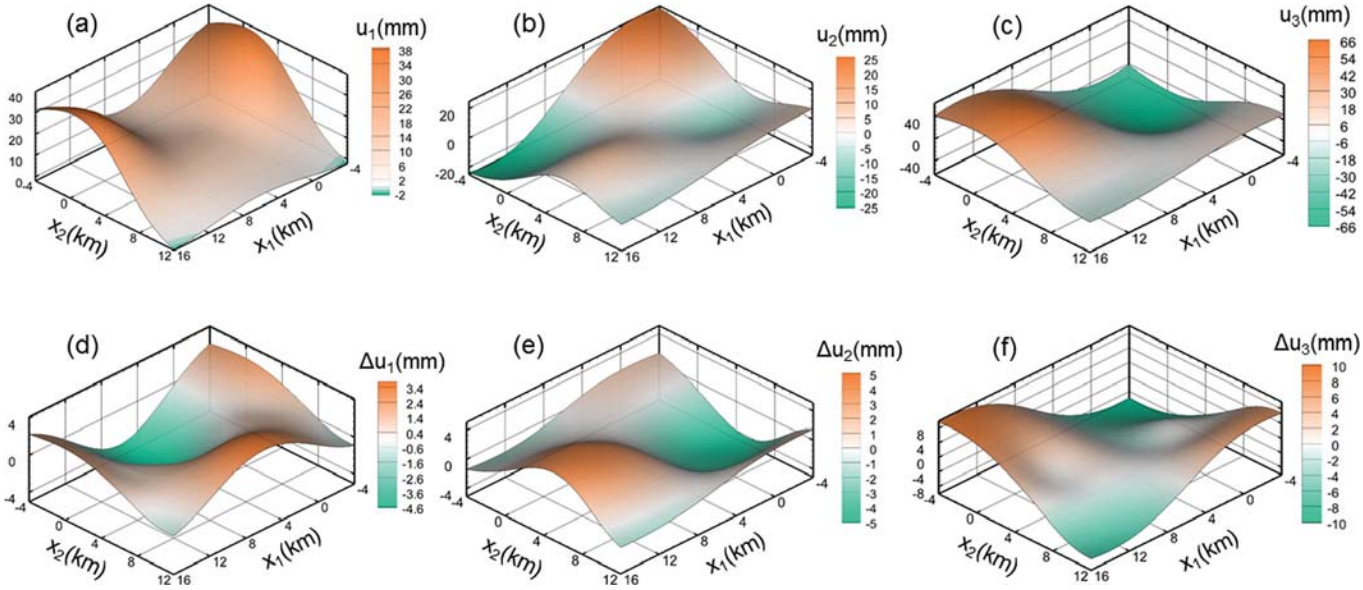

Figure 7. Surface deformation due to a strike-slip fault in a viscoelastic TIV half-space. Top row (a–c) shows the viscoelastic deformation on the surface at normalized time $t/\tau^1_{\varepsilon 1} = 4.5$ and the bottom row (d–f) shows the difference between the elastic and viscoelastic deformations. (Multimedia view).

increases, although their rate of convergence is slower as compared to that of displacements.

As a final numerical example, we present the surface response induced by different types of faults. The geometry of the problem is the same as the one shown in Fig. 4 and the observation area is a rectangle on the surface of the half-space with -4 km $< x_1 < 16$ km and -4 km $< x_2 < 12$ km. The surface responses for the strike-slip fault, dip-slip fault and tensile fracture are shown in Figs 7–9, respectively. In these figures, the top row is the surface response at the normalized time $t/\tau^1_{\varepsilon 1} = 4.5$ where the displacement components converge to their limiting values and the bottom row is the difference between the elastic and viscoelastic responses. It can be observed from Fig. 7a that the displacement component u_1 due to a strike-slip fault is nearly all positive in the entire domain whilst the difference between the elastic and viscoelastic responses could be positive or negative (Fig. 7d). A similar feature can be observed for the displacement component u_3 by a tensile fault shown in Figs 9(c) and (f). It is further noticed from the bottom rows of Figs 7–9 that the difference between the elastic and viscoelastic deformations could be significant. This is particularly true for the vertical displacement where the difference is in the same order of the actual deformation (Fig. 8f). All these observations indicate that both transverse isotropy and viscoelasticity play an important role in the prediction of displacement and stress fields. Thus for more realistic and accurate predictions, viscoelasticity and anisotropy must be considered especially for sedimentary rock masses.

4 CONCLUSIONS

We have derived the time-dependent displacement and stress fields induced by faults in a viscoelastic half-space. Utilizing the correspondence principle, we first find the solutions in the Laplace domain. Using an accurate and efficient inverse Laplace transform algorithm, we obtain the solutions in the time domain. The formulations are applied to a TIV half-space and two IV half-spaces with three types of finite-size faults. Our viscoelastic solutions at $t = 0$ are validated with the elastic solutions for both isotropic and transversely isotropic case, and at any time t, are validated with the analytical solutions by Singh & Rosenman (1974) for the simple Maxwell model. Our numerical results show the following important features:

(1) For a given fault, variations of the viscoelastic displacement and stress fields with time can be completely different in TIV and IV half-spaces.

(2) The magnitude of the difference between the elastic and viscoelastic fields can be significant, especially when the half-space is deformed by dip-slip and tensile faults.

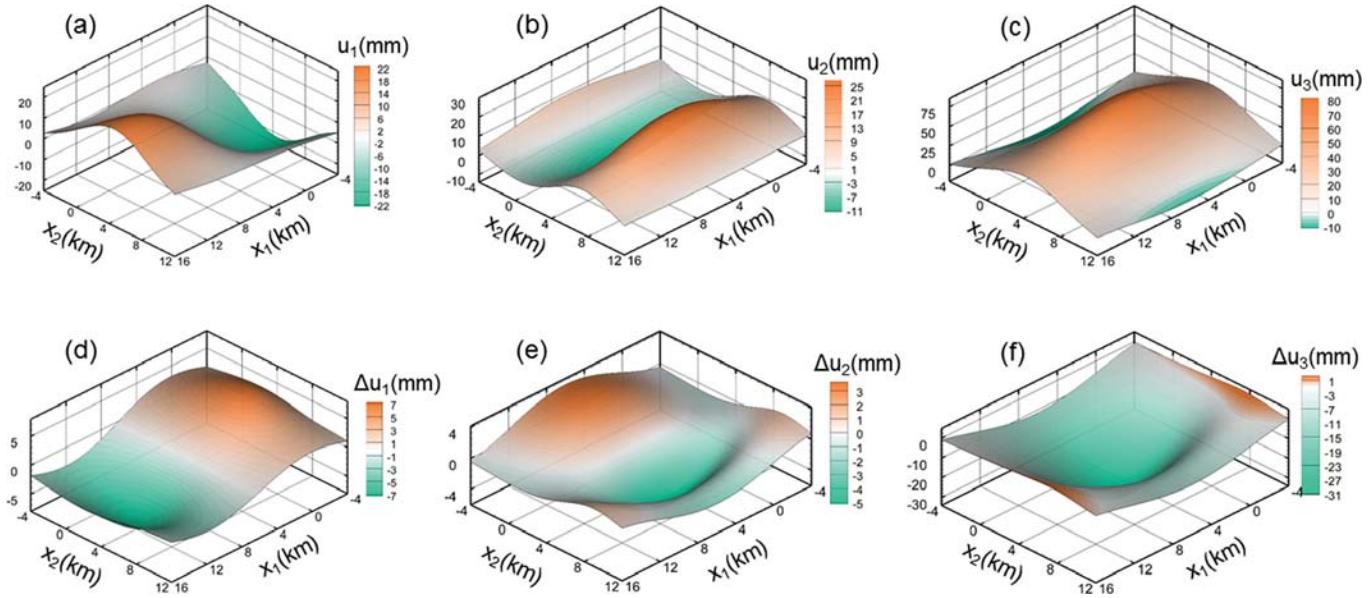

Figure 8. Surface deformation due to a dip-slip fault in a viscoelastic TIV half-space. The top row (a–c) shows the viscoelastic deformation on the surface at normalized time $t/\tau_{\varepsilon 1}^{1} = 4.5$ and the bottom row (d–f) shows the difference between the elastic and viscoelastic deformations. (Multimedia view).

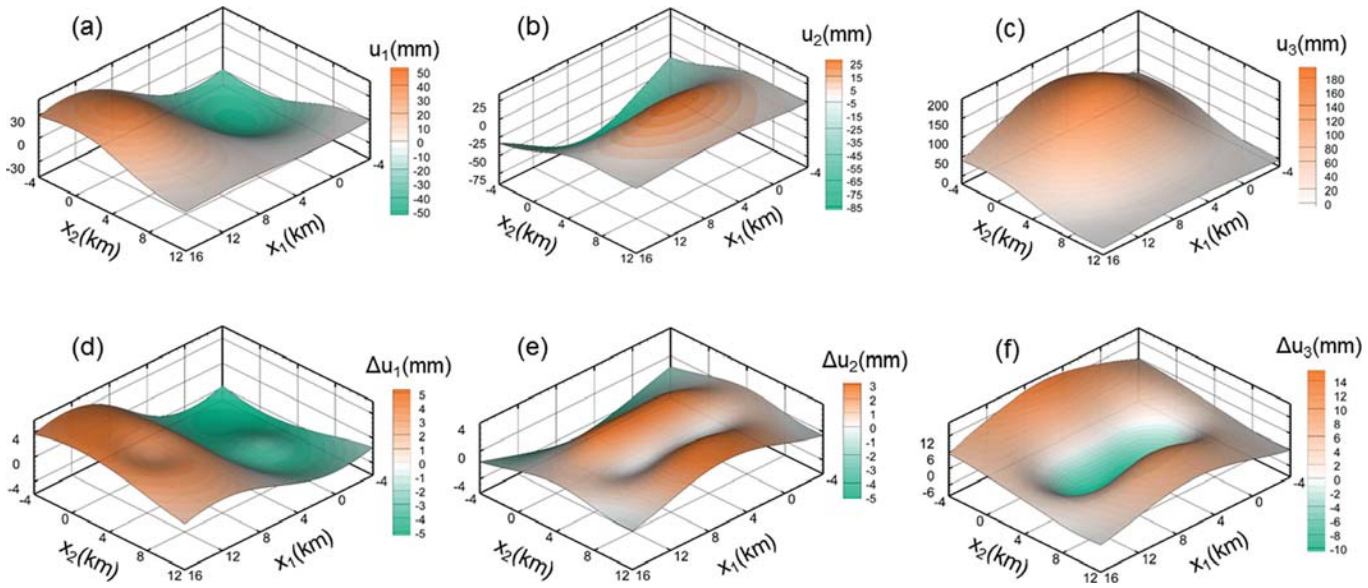

Figure 9. Surface deformation due to a tensile fault in a viscoelastic TIV half-space. The top row (a–c) shows the viscoelastic deformation on the surface at normalized time $t/\tau_{\varepsilon 1}^{1} = 4.5$ and the bottom row (d–f) shows the difference between the elastic and viscoelastic deformation. (Multimedia view).

(3) In a viscoelastic half-space, the maximum values of the hydrostatic stress, effective stress, and the maximum shear stress induced by a given fault do not occur in the elastic limit. They all increase with increasing time, implying possible post-seismic failure in rocks.

In summary, our numerical results demonstrate that one may need to consider both elastic anisotropy and viscoelastic anisotropy in materials in order to predict accurately the deformation and stress fields in the lithosphere due to a post-seismic or volcanic event.

ACKNOWLEDGEMENTS

The authors would like to thank Prof. Bert Vermeersen and the two reviewers for their constructive comments on the original version of the paper. A. Sangghaleh has also provided beneficial comments on the original and revised versions of the paper. This work is partially supported by the United States National Institute for Occupational Health and Safety Award # 1R03OH010112–01A1.

REFERENCES

Amadei, B., 1996. Importance of anisotropy when estimating and measuring *in situ* stresses in rock. *Int. J. Rock Mech. Min. Geomech. Abstr.,* **33,** 293–325.

Bellman, R., Kalaba, R.E. & Lockett, J.A., 1966. *Numerical Inversion of the Laplace Transform: Applications to Biology, Economics, Engineering, and Physics,* **Vol. 4,** American Elsevier Publishing Company.

Bracewell, R.N., 1978. *The Fourier Transform and its Applications,* 2nd edn, McGraw-Hill.

Carcione, J.M., 1990. Wave propagation in anisotropic linear viscoelastic media: theory and simulated wavefields. *Geophys. J. Int.,* **101,** 739–750.

Carcione, J.M., Kosloff, D. & Kosloff, R., 1988. Wave propagation simulation in a linear viscoelastic medium. *Geophys. J. Int.,* **95,** 597–611.
Chen, E.Y., Pan, E. & Green, R., 2009. Surface loading of a multilayered viscoelastic pavement: Semianalytical solution. *J. Eng. Mech.,* **135,** 517–528.
Christensen, R., 1982. *Theory of Viscoelasticity: An Introduction*. American Elsevier Publishing Company.
Cohen, A.M., 2007. *Numerical Methods for Laplace Transform Inversion,* **Vol. 5,** Springer-Verlag.
Davies, B. & Martin, B., 1979. Numerical inversion of the Laplace transform: a survey and comparison of methods. *J. Comput. Phys.,* **33,** 1–32.
De Hoog, F.R., Knight, J.H. & Stokes, A.N., 1982. An improved method for numerical inversion of Laplace transforms. *SIAM J. Sci. Comput.,* **3,** 357–366.
Dubner, H. & Abate, J., 1968. Numerical inversion of Laplace transforms by relating them to the finite Fourier cosine transform. *J. ACM,* **15,** 115–123.
Duffy, D.G., 1993. On the numerical inversion of Laplace transforms: comparison of three new methods on characteristic problems from applications. *ACM T Math. Software,* **19,** 333–359.
Durbin, F., 1974. Numerical inversion of Laplace transforms: an efficient improvement to Dubner and Abate's method. *Comput. J.,* **17,** 371–376.
Fialko, Y., 2004. Evidence of fluid-filled upper crust from observations of postseismic deformation due to the 1992 Mw7. 3 Landers earthquake. *J. geophys. Res.: Solid Earth,* **109,** B08401, doi:10.1029/2004JB002985.
Gercek, H., 2007. Poisson's ratio values for rocks. *Int. J. Rock Mech. Min. Sci.,* **44,** 1–13.
Hetland, E.A. & Hager, B.H., 2005. Postseismic and interseismic displacements near a strike-slip fault: a two-dimensional theory for general linear viscoelastic rheologies. *J. geophys. Res.: Solid Earth,* **110,** B10401, doi:10.1029/2005JB003689.
Hetland, E.A. & Hager, B.H., 2006. The effects of rheological layering on post-seismic deformation. *Geophys. J. Int.,* **166,** 277–292.
Honig, G. & Hirdes, U., 1984. A method for the numerical inversion of Laplace transforms. *J. Comput. Appl. Math.,* **10,** 113–132.
Knauss, W.G., 1970. Delayed failure—the Griffith problem for linearly viscoelastic materials. *Int. J. Fract. Mech.,* **6,** 7–20.
Kuhlman, K.L., 2013. Review of inverse Laplace transform algorithms for Laplace-space numerical approaches. *Numer. Algorithms,* **63,** 339–355.
Nur, A. & Mavko, G., 1974. Postseismic viscoelastic rebound. *Science,* **183,** 204–206.
Okada, Y., 1985. Surface deformation due to shear and tensile faults in a half-space. *Bull. seism. Soc. Am.,* **75,** 1135–1154.
Okada, Y., 1992. Internal deformation due to shear and tensile faults in a half-space. *Bull. seism. Soc. Am.,* **82,** 1018–1040.
Pan, E., Yuan, J.H., Chen, W.Q. & Griffith, W.A., 2014. Elastic deformation due to polygonal dislocations in a transversely isotropic half-space. *Bull. seism. Soc. Am.,* **104,** 2698–2716.
Piombo, A., Tallarico, A. & Dragoni, M., 2007. Displacement, strain and stress fields due to shear and tensile dislocations in a viscoelastic half-space. *Geophys. J. Int.,* **170,** 1399–1417.
Singh, S.J. & Rosenman, M., 1974. Quasi-static deformation of a viscoelastic half-space by a displacement dislocation. *Phys. Earth planet. Inter.,* **8,** 87–101.
Stehfest, H., 1970. Algorithm 368: numerical inversion of Laplace transforms [D5]. *Commun. ACM,* **13,** 47–49.
Talbot, A., 1979. The accurate numerical inversion of Laplace transforms. *IMA J. Appl. Math.,* **23,** 97–120.
Wang, C.D. & Liao, J.J., 1998. Stress influence charts for transversely isotropic rocks. *Int. J. Rock Mech. Min. Sci.,* **35,** 771–785.
Weeks, W.T., 1966. Numerical inversion of Laplace transforms using Laguerre functions. *J. ACM,* **13,** 419–429.
Williams, J., 1973. *Laplace Transforms, Problem Solvers*. George Allen & Unwin.
Wnuk, M.P. & Knauss, W.G., 1970. Delayed fracture in viscoelastic-plastic solids. *Int. J. Solids Struct.,* **6,** 995–1009.

APPENDIX: VALIDATION AND EFFICIENCY OF NUMERICAL LAPLACE INVERSE TRANSFORM ALGORITHHM

We investigate the accuracy and efficiency of the inverse Laplace transform by looking at the following three typical and oscillating decaying functions

$$f_1(t) = J_3(2t)H(t); \quad f_2(t) = \mathrm{e}^{-2t}\cos(3t)H(t);$$
$$f_3(t) = \mathrm{e}^{-2t}\sin(3t)H(t). \tag{A1}$$

The Laplace transform of these functions are (Williams 1973; Bracewell 1978),

$$F_1(s) = \frac{(\sqrt{s^2+4}-s)^3}{8\sqrt{s^2+4}}; \quad F_2(s) = \frac{s-2}{(s+2)^2+9};$$
$$F_3(s) = \frac{3}{(s+2)^2+9}. \tag{A2}$$

To carry out the inverse Laplace transform of eq. (A1), we apply eq. (23) with $N = 60$ as suggested by Honig & Hirdes (1984). While the other two parameters (κ and T) are optimally found in the algorithm, we use the ϵ-algorithm and curve fitting method simultaneously to accelerate the convergence of the Fourier series expansion. Our code was written in Matlab® R2014b on a macbook pro laptop with 2.3 GHz Intel Core i5 processor and 4GB 1333 MHz DDR3 ram platform. The decaying functions in eq. (A1) versus time are plotted in Fig. 2 and are compared with the results obtained via the numerical Laplace inverse transform algorithm of eq. (A2). The results indicate that the exact and numerical solutions are in good agreement for these decaying functions. While the maximum relative error for the Bessel function f_1 is about 10^{-8}, the relative errors for f_2 and f_3 are about 4.1×10^{-4} and 1.7×10^{-3}. It is observed from Fig. A1 that the maximum relative error for f_2 and f_3 occurs at the starting time and it decays to zero as the magnitude of the functions goes to zero. In addition, for each decaying function, the runtime for 100 discrete time points is also calculated. It is observed that for the Bessel function f_1, the calculation time was 1.03 s while for functions f_2 and f_3, the runtimes were 0.79 and 0.81 s, respectively. The relative errors and the presented computational time demonstrate the accuracy and efficiency of the inverse Laplace transform algorithm. In the examples presented in this paper, the same procedure as discussed above is used for the numerical inverse Laplace transform.

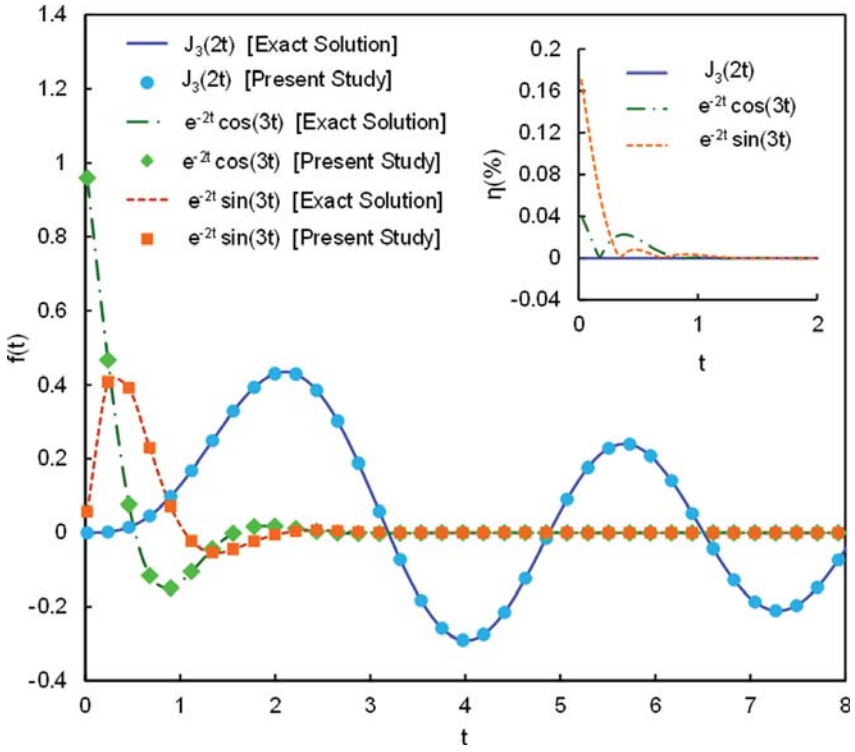

Figure A1. Comparison of the present numerical inverse Laplace transform algorithm based on Honig & Hirdes (1984) with the exact solutions for three different oscillating decaying functions. The inset shows the relative percentage error (η) of each function $f(t)$ versus dimensionless time t.

SUPPORTING INFORMATION

Additional Supporting Information may be found in the online version of this article:

Figure S7. Surface deformation versus normalized time (from 0 to 4.5) due to a strike-slip fault in a viscoelastic TIV half-space. The top row shows the viscoelastic deformation on the surface versus time and the bottom row shows the difference between the elastic and viscoelastic deformations versus time.

Figure S8. Surface deformation versus normalized time (from 0 to 4.5) due to a dip-slip fault in a viscoelastic TIV half-space. The top row shows the viscoelastic deformation on the surface versus time and the bottom row shows the difference between the elastic and viscoelastic deformations versus time.

Figure S9. Surface deformation versus normalized time (from 0 to 4.5) due to a tensile fault in a viscoelastic TIV half-space. The top row shows the viscoelastic deformation on the surface versus time and the bottom row shows the difference between the elastic and viscoelastic deformations versus time (http://gji.oxfordjournals.org/lookup/suppl/doi:10.1093/gji/ggv115/-/DC1)

Please note: Oxford University Press are not responsible for the content or functionality of any supporting materials supplied by the authors. Any queries (other than missing material) should be directed to the corresponding author for the article.